Updated reaction rate of ^{25}Mg(p, γ)^{26}Al and its astrophysical implication

H. Zhang [1] J. Su,[1,2,3,*] Z. H. Li,[2,4,†] Y. J. Li,[2] E. T. Li,[5,‡] C. Chen,[2] J. J. He [1,3] Y. P. Shen [2] G. Lian,[2] B. Guo,[2] X. Y. Li,[1] L. Y. Zhang,[1,3] Y. D. Sheng,[1] Y. J. Chen,[1] L. H. Wang,[1] L. Zhang,[2] F. Q. Cao,[2] W. Nan [2] W. K. Nan,[2] G. X. Li,[2] N. Song,[2] B. Q. Cui,[2] L. H. Chen,[2] R. G. Ma,[2] Z. C. Zhang,[2] T. Y. Jiao,[6] B. S. Gao [6] X. D. Tang,[6] Q. Wu,[6] J. Q. Li,[6] L. T. Sun,[6] S. Wang,[7] S. Q. Yan,[2] J. H. Liao,[2] Y. B. Wang [2] S. Zeng,[2] D. Nan,[2] Q. W. Fan,[2] and W. P. Liu[2,8]

[1]*Key Laboratory of Beam Technology of Ministry of Education, College of Nuclear Science and Technology, Beijing Normal University, Beijing 100875, China*

[2]*China Institute of Atomic Energy, P. O. Box 275(10), Beijing 102413, China*

[3]*Institute of Radiation Technology, Beijing Academy of Science and Technology, Beijing 100875, China*

[4]*School of Nuclear Science and Technology, University of Chinese Academy of Sciences, Beijing 101408, China*

[5]*Institute for Advanced Study in Nuclear Energy and Safety, College of Physics and Optoelectronic Engineering, Shenzhen University, Shenzhen 518060, China*

[6]*Institute of Modern Physics, Chinese Academy of Sciences, Lanzhou 730000, China*

[7]*Shandong Provincial Key Laboratory of Optical Astronomy and Solar-Terrestrial Environment, Institute of Space Sciences, Shandong University, Weihai 264209, China*

[8]*College of Science, Southern University of Science and Technology, Shenzhen 518055, China*

(Received 19 December 2022; revised 22 March 2023; accepted 24 April 2023; published 5 June 2023)

^{26}Al with a half-life of 7.17×10^5 years is one of the most significant nuclides in γ-ray astronomy and presolar grains of meteorites. Its main production mechanism in the H-burning MgAl cycle is the ^{25}Mg(p, γ)^{26}Al reaction. In the temperature region of 0.05–0.3 GK of astrophysical interest, the astrophysical ^{25}Mg(p, γ)^{26}Al reaction rate is dominated by the resonant capture of several low-energy resonances. In this work, we report the results of a complete experimental investigation of the $E_{\rm c.m.} = 92$, 130, and 189 keV resonances in the ^{25}Mg(p, γ)^{26}Al reaction with the Jinping Underground Nuclear Astrophysics Experimental Facility. The updated thermonuclear ^{25}Mg(p, γ)^{26}Al reaction rate is (32–39)% higher than that obtained at the Laboratory for Underground Nuclear Astrophysics around 0.07–0.09 GK, mainly due to the 32% enhancement of the 92-keV resonance strength. The astrophysical impact of our new rate on the ^{26}Al yield in a 5 $M_\odot$ low-metallicity asymptotic giant branch star is investigated, in which an increase of (45–79)% in the ^{26}Al yield is found by adopting our new ^{25}Mg(p, γ)^{26}Al rates.

DOI: 10.1103/PhysRevC.107.065801

I. INTRODUCTION

Since the 1.809 MeV γ-ray line emitted by the radioactive decay of the ground state of ^{26}Al (hereinafter expressed as ^{26}Al$^{\rm g}$) in the galaxy was first observed by the HEAO-3 satellite [1], great efforts [2,3] have been made, which have revealed the presence of 2.8 ± 0.8 $M_\odot$ ^{26}Al in the interstellar medium [3]. In view of the lifetime of ^{26}Al$^{\rm g}$ ($T_{1/2} = 7.17\times10^5$ yr) being much shorter than the galactic evolution ($\approx 10^{10}$ yr), discovery of the 1.809 MeV γ-ray line provides a convincing evidence that the nucleosynthesis of ^{26}Al is ongoing in our galaxy. Signs of ^{26}Al have been also found through the excess of ^{26}Mg in meteorites [4,5], some of them provide evidence for the injection of live ^{26}Al in the early solar system [6], and some provide information on nucleosynthesis that occurred in the parent stars of meteoritic stardust [5,7]. Additionally, ^{26}Al is also linked to the Mg–Al anticorrelation observed globular clusters, with metal-poor massive asymptotic giant branch (AGB) stars as possible polluters [8].

Over the past decades, several stellar sites for the nucleosynthesis of ^{26}Al have been identified, e.g., the core of massive main-sequence stars [9], the H-burning shell of red giant branch (RGB) stars [10] and AGB stars [11], as well as red supergiant stars [12] and binary stars [13,14]. In these environments, the MgAl reaction cycle is very important for ^{26}Al, which is produced via the ^{25}Mg(p, γ)^{26}Al reaction and destroyed by β^+ decay or the ^{26}Al(p, γ)^{27}Si reaction [15]. Therefore, the ^{25}Mg(p, γ)^{26}Al reaction plays an important role in the study of the origin of ^{26}Al.

At astrophysical relevant temperatures from 0.05 to 0.3 GK, the reaction rate of ^{25}Mg(p, γ)^{26}Al is dominated by several narrow resonances in the center-of-mass energy range of $E_{\rm c.m.} = 30$–400 keV. Among them, the 304-keV resonance has been well studied in previous direct and indirect measurements [16–27]. For the 189-keV resonance, instead, the latest direct measurement result of $\omega\gamma_{189} = (9.0 \pm 0.6)\times10^{-7}$ eV [28] differs from the NACRE [29] value of

*sujun@bnu.edu.cn
†zhli@ciae.ac.cn
‡let@szu.edu.cn

$(7.1 \pm 1.0)\times10^{-7}$ eV by about 30%, which is mainly caused by the discrepancy in the primary γ-ray branching ratios. For the 130-keV resonance, due to its weak strength and the interference from other reactions, there are only upper limits in the literature [28,29]. Finally, for the 92-keV resonance, the only direct measurement experiment [28] gave a resonance strength of $\omega\gamma_{92} = (2.9 \pm 0.6)\times10^{-10}$ eV, with a ground-state feeding factor of $f_0^{92} = 0.6^{+0.2}_{-0.1}$. More recent indirect measurements [30,31] reported two different values of 0.52 ± 0.06 and 0.76 ± 0.1, consistent only within 1.4σ confidence intervals. In summary, all these uncertain physical quantities significantly limit the current precision of the astrophysical ^{25}Mg$(p,\gamma)^{26}$Al reaction rate and provide motivation to further studies via new direct measurement.

In this article, we report on the complete results of a direct measurement of the low-energy resonances in the ^{25}Mg$(p,\gamma)^{26}$Al reaction using Jinping Underground Nuclear Astrophysics experimental facility (JUNA) [32]. JUNA is located at the China JinPing underground Laboratory (CJPL) [33], the deepest operational underground laboratory for particle and nuclear physics experiments in the world. Shielded by the 2400-m overburden marble, the muon and neutron background are reduced by eight and four orders of magnitude, respectively, as compared to the flux on the earth surface [33–35]. The experimental results on the strength and branching ratios of the 92-keV resonance were reported in our previous publication [36]. In addition, in the present paper we present an investigation of the astrophysical impact of our updated ^{25}Mg$(p,\gamma)^{26}$Al reaction rates on a 5 $M_\odot$ low-metallicity AGB star.

II. EXPERIMENT

A. Experiment setup

The experiment was performed on a high-current 400 kV JUNA accelerator, which can provide H^+ and He^+ beams up to 10 emA, as well as a He^{2+} beam up to 2 emA [37]. In this work, the ^{25}Mg$(p,\gamma)^{26}$Al reaction was studied in an energy range of $E_p = 117$–350 keV with a proton beam up to 2 mA. The experimental setup was described in Refs. [36,38,39]. Briefly, the proton beam was guided by two tantalum apertures and a copper cold trap, then illuminated the target with a beam spot of about 2 cm^2 size. The target was placed at 0° with respect to the beam direction and cooled directly by the deionized water. The trap was cooled by liquid nitrogen (LN_2) to minimize carbon deposition on the target surface. The target and the end of the vacuum tube together formed a Faraday cup for charge integration. A ring electrode applied with a negative voltage of 300 V was installed between the target and cold trap to suppress the secondary electron emission. The JUNA 400 kV accelerator was calibrated by measuring the yield curves of the ^{11}B$(p,\gamma)^{12}$C, ^{14}N$(p,\gamma)^{15}$O, ^{27}Al$(p,\gamma)^{28}$Si resonances and the γ-ray energy of ^{12}C$(p,\gamma)^{13}$N. The absolute energy was determined to an accuracy of 0.5 keV with an energy spread of less than 0.2 keV, the detail results of accelerator calibration will be published elsewhere [40].

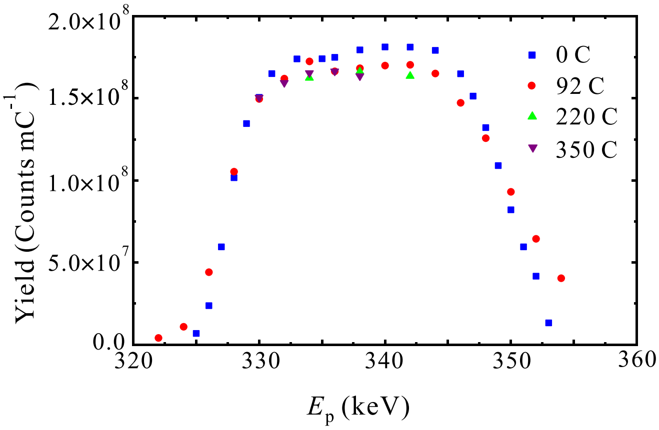

FIG. 1. Yield curves for the 304-keV resonance at the beginning of the experiment (i.e., 0 C, blue square), and after 92 C (red circle), 220 C (green triangle), and 350 C (purple inverted triangle) proton beam bombardment, respectively.

B. Target

The ^{25}Mg targets used in this experiment were evaporated from ^{25}Mg isotope enriched metal ($98.81\% \pm 0.02\%$ abundance) onto a copper substrate with a diameter of Φ47.5 mm. The thickness of the target was set to be $\approx$60 μg/cm^2, i.e., the energy loss was 23 keV at $E_p = 316$ keV. A Cr protective layer with a thickness of $\approx$40 μg/cm^2 (energy loss of 10 keV at $E_p = 316$ keV) was sputtered on the surface of each target to enhance the radiation resistance of the target [41]. The stoichiometry was mainly composed of magnesium and oxygen, and the effective stopping power was calculated by a SRIM code [42]. In addition, several natural Mg targets with the same structure and thickness were fabricated to evaluate the background induced by the (p,γ) reactions on the target contaminants, such as ^{7}Li, ^{10,11}B, and ^{24,26}Mg.

In order to accurately measure the radiation damage of the target under high intensity beam bombardment, the target stoichiometry was monitored during the experiment by scanning the yield curve of the $E_p = 304$ keV resonance every $\approx$100 Coulomb beam (Fig. 1). This stoichiometry information was used in the subsequent data analysis to obtain the effective stopping power as described in detail in Sec. III A. The observed largest decrease of the maximum yield was $\approx$11% after 350 Coulomb beam bombardment, which is much improved compared with that reported in Ref. [26].

C. Detector

The emitted γ rays were detected by a nearby 4π geometry BGO detector array composed of eight identical segments. Each crystal is a quadrangular prism with a length of 250 mm and a radial thickness of 63 mm, covering an azimuthal angle of 45°. In order to improve the energy resolution of the detector, all BGO crystals were cooled to about –10 °C [27] by flowing low-temperature alcohol in the cooper substrates installed outside of each crystal. Additionally, the detector was surrounded by 5 mm Cu, 100 mm Pb, and 1 mm Cr shielding to reduce the background from environmental radiation.

Two kinds of energy spectra can be obtained with the BGO detector array: one is the single spectrum, which is the count superposition of eight spectra obtained by all BGO segments, and another is the sum spectrum representing the sum of the energies measured by eight BGO segments. The BGO detector array was calibrated by two point-like γ-ray sources (^{60}Co and ^{137}Cs), as well as the $E_{\rm c.m.} = 293$ keV resonance of the ^{27}Al$(p,\gamma)^{28}$Si reaction. The energy resolution was found to be 11.9%, 8.4%, and 4% at $E_\gamma = 662$, 1333, and 7249 keV in the single spectra of the ^{60}Co, ^{137}Cs sources and the ^{27}Al$(p,\gamma)^{28}$Si reaction, respectively. Furthermore, the efficiency of the BGO sum spectrum was simulated with a GEANT4 code [43]. The simulation was validated by measurements of two standard γ-ray sources, where the efficiencies of the sum peaks of the ^{137}Cs and ^{60}Co sources were determined to be 57(1)% and 31(1)%, respectively.

III. RESULTS

A. Analysis method

The data was analyzed by a γ-summing method [44,45]. The advantages of the γ-summing method are the relatively high efficiency and the nearly 4π geometry. The former enables the measurement of extremely low cross-section reactions possible, while the latter could minimize the angular distribution and angular correlation effects [46]. In the γ-summing method, the characteristic sum peak of the targeted reaction can be usually identified easily in the sum spectrum and then used to determine the reaction yield by

$$Y = \frac{N_{\rm sum}}{\epsilon_{\rm sum}}, \qquad (1)$$

where $N_{\rm sum}$ is the counts of the sum peak and $\epsilon_{\rm sum}$ is the efficiency of the sum peak (i.e., the summing efficiency). Different from that of the single γ ray, the summing efficiency of the cascade γ transition depends not only on the detector geometry and experiment setup but also on the decay scheme of the transition, especially for that with high multiplicity. Therefore, an accurate decay scheme of the resonance is necessary for the precise determination of the summing efficiency as well as the yield of the resonance.

In this work, we extracted the decay scheme from the single spectrum obtained by the BGO detector array. To suppress the background raised by environmental radioactivity and (p,γ) reactions of contaminants in the target, the single spectrum was produced by setting an energy window on the sum peak in the sum spectrum with a width of 800 keV. A Bayesian method based on the Bayesian Analysis Toolkit [47] was utilized to extract the decay scheme of the resonance from the single spectrum.

The Bayesian method takes the counts of each primary γ-ray branch in the ^{25}Mg$(p,\gamma)^{26}$Al reaction as a posterior probability, which is a binned likelihood that assumes the fluctuations in each bin are Poisson-like and independent of each other. Then, the posterior probability is compared with the prior distribution, i.e., both the single and sum spectrum obtained from the experiment, and the possible values for parameters within a model are given.

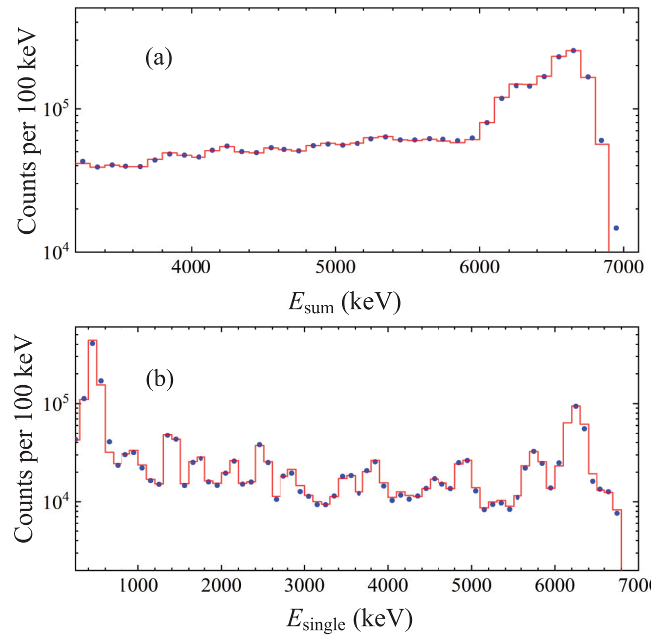

FIG. 2. γ-ray spectra of the 304-keV resonance (in blue circles). (a) Sum spectrum; (b) single spectrum. The red lines represent fitting results.

Figure 2(a) shows the sum spectrum of the 304-keV resonance, and Fig. 2(b) shows the single spectrum by putting a 6200–7000 keV gate on the sum peak. The primary γ-ray branching ratios for the 304-keV resonance were extracted by fitting the sum and single spectrum via the Bayesian method, as shown in Fig. 2. The present results are compared with those obtained with HPGe detectors in Table I. The transitions with low branching ratios cannot be reproduced, and several transitions to near excited states cannot be well distinguished. This is mainly due to the limitations of the energy resolution of the BGO detector and the high multiplicity of the cascade transition. However, the present methods is able to derive the dominant branching ratios, and the fitting result can well reproduce the sum and single spectrum, as shown in Fig. 2, meanwhile, since the background contribution is more than three orders of magnitude smaller than that of the 304-keV resonance, the uncertainty of subtracting the background is negligible.

In the case of measuring narrow resonances with a thick target, the resonance strength $\omega\gamma$ can be determined by measuring the maximum yield $Y_{\rm max}$ [48],

$$Y_{\rm max} = \frac{\lambda^2}{2}\frac{M+m}{M}\frac{1}{\varepsilon_{\rm eff}}\omega\gamma, \qquad (2)$$

where λ and $\varepsilon_{\rm eff}$ represent the de Broglie wavelength and the effective stopping power of proton in the target, M and m are the atomic masses of ^{25}Mg and proton, respectively. Since the 304-keV resonance was studied precisely in the previous work [27], the recommended resonance strength $\omega\gamma_{304} = 31.0 \pm 1.0$ meV can be used as a reference to calculate the lower energy resonances. In the present relative measurement, the strengths of the 189, 130, and 92 keV resonances were

TABLE I. Primary γ-ray branching ratios (in %) for the 304-keV resonance of the $^{25}Mg(p,\gamma)^{26}Al$ reaction.

E_x	Present work	Ref. [27]	Ref. [26]
5916		0.07 ± 0.02	0.09 ± 0.02
5726		0.09 ± 0.02	0.10 ± 0.01
5457		0.15 ± 0.06	
5396		0.24 ± 0.03	0.22 ± 0.02
4940		0.12 ± 0.07	0.08 ± 0.01
4622	1.7 ± 0.2	0.27 ± 0.11	0.28 ± 0.07
4599		0.11 ± 0.03	0.12 ± 0.01
4548		1.26 ± 0.08	1.30 ± 0.07
4349			0.03 ± 0.01
4206	2.9 ± 0.3	0.18 ± 0.04	0.25 ± 0.02
4192	16.7 ± 1.7	18.9 ± 0.3	19.1 ± 0.3
3963		0.18 ± 0.03	0.17 ± 0.01
3751	2.5 ± 0.3	0.90 ± 0.05	0.92 ± 0.02
3681		1.02 ± 0.05	1.09 ± 0.03
3675		0.92 ± 0.13	0.86 ± 0.13
3596	5.0 ± 0.5	4.31 ± 0.20	4.29 ± 0.07
3160	11.1 ± 1.1	11.3 ± 0.05	11.4 ± 0.2
3074		0.13 ± 0.05	0.11 ± 0.04
2913	2.0 ± 0.2	3.07 ± 0.14	3.04 ± 0.05
2661		1.06 ± 0.06	1.00 ± 0.02
2545	3.9 ± 0.4	1.45 ± 0.03	1.46 ± 0.03
2365		0.37 ± 0.05	0.47 ± 0.02
2069	5.9 ± 0.6	6.3 ± 0.1	6.0 ± 0.1
1759	15.5 ± 1.5	15.8 ± 0.3	16.1 ± 0.3
417	33.0 ± 3.3	31.7 ± 0.4	31.8 ± 0.5
0			0.058 ± 0.004

obtained by the following expression:

$$\omega\gamma = \frac{\lambda^2(304)}{\lambda^2}\frac{A/\eta}{A_{304}/\eta_{304}}\frac{N_{304}}{N}\frac{\varepsilon_{\rm eff}}{\varepsilon_{\rm eff}(304)}\omega\gamma_{304}, \quad (3)$$

where A, η, and N are the sum peak count, sum peak efficiency, and proton numbers in the corresponding resonance measurement, respectively. In the present analysis, the sum spectra of GEANT4 simulations were fitted to the experimental spectra by normalized scale, the sum peak counts A were obtained from the scale factor and the total event number generated in the GEANT4 simulation, and the efficiency η was determined by the full decay scheme. Considering the main components of the target, the effective stopping power of Mg targets $\varepsilon_{\rm eff}$ is given by

$$\varepsilon_{\rm eff} = \varepsilon_{\rm Mg} + \frac{N_{\rm O}}{N_{\rm Mg}}\varepsilon_{\rm O}, \quad (4)$$

where $N_{\rm O}$ and $N_{\rm Mg}$ are the number densities of oxygen and magnesium in the targets, respectively. The effective stopping power $\varepsilon_{\rm eff}$ is affected by the stoichiometry of ^{25}Mg target, and the ratios $\varepsilon_{\rm eff}/\varepsilon_{\rm eff}(304)$ were calculated with an O abundance of 22% [27]. To investigate the effect of the O/Mg ratios change during the strong proton beam bombardment, the effective stopping power ratio $\varepsilon_{\rm eff}/\varepsilon_{\rm eff}(304)$ was calculated over a large range of O/Mg ratios, revealing a maximum $\varepsilon_{\rm eff}/\varepsilon_{\rm eff}(304)$ variation of 1.2%.

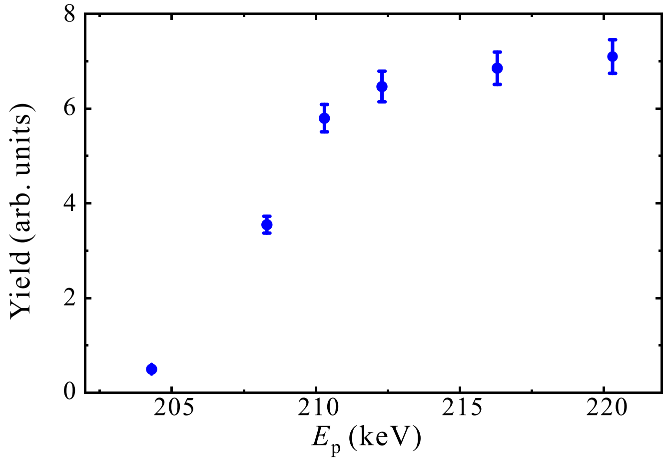

FIG. 3. Yield curve measured for the 189-keV resonance.

B. The 189-keV resonance

Figure 3 shows the yield curve measured for the 189-keV resonance over a proton energy E_p range between 204 and 220 keV, with a proton beam intensity of about 1 mA. The stoichiometry change was found to be 11% by scanning the 304-keV resonance before and after the measurement. At the top of the plateau, the spectrum at the $E_p = 216.3$ keV run was used to obtain the resonance strength and branching ratios.

The sum spectrum with a total charge of 3.6 C is shown in Fig. 4(a), while the single spectrum obtained by putting a 6000–6800 keV gate on the sum peak is shown in Fig. 4(b). The beam-induced background mainly consists

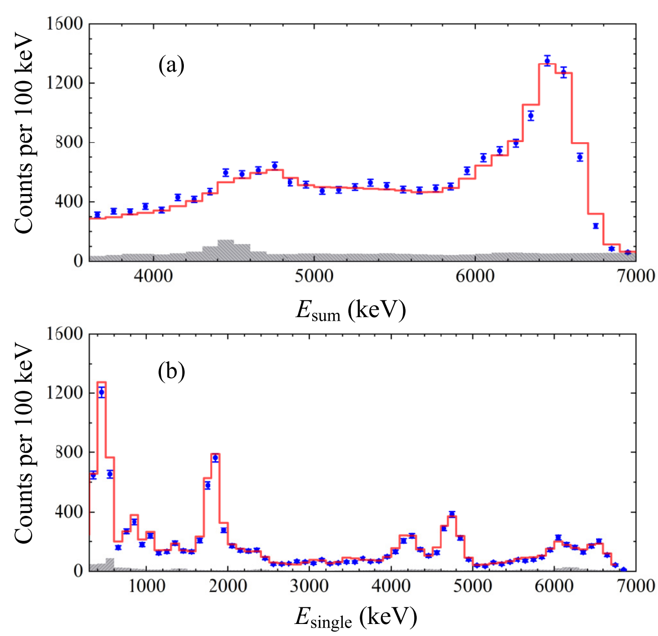

FIG. 4. γ-ray spectra of the 189-keV resonance (in blue circles). (a) Sum spectrum, where the shadowed area represents the background; (b) single spectrum. The line represents the fitting result using the Bayesian method, while the shadowed area represents the background.

TABLE II. Primary γ-ray branching ratios for the 189-keV resonance of the ^{25}Mg$(p,\gamma)^{26}$Al reaction.

E_x	Present	Ref. [28]	Ref. [23]	Ref. [20]
5583			8 ± 2	
5726	4.9 ± 0.7	3.0 ± 1.0	7 ± 2	
4705	48.2 ± 4.9	48.7 ± 2.0	35 ± 4	50 ± 2
3403	2.4 ± 0.4	1.5 ± 0.5		4.5 ± 0.9
3074	5.9 ± 1.1	1.4 ± 0.5	<4	
2545	5.5 ± 1.1	7.7 ± 1.0	12 ± 4	5.8 ± 1.2
2365	18.3 ± 2.1	21.9 ± 2.0	26 ± 4	19 ± 1
417	8.5 ± 0.9	10.2 ± 1.0	12 ± 4	21 ± 3
0	6.3 ± 0.7	5.6 ± 1.1		

of the ^{11}B$(p,\gamma)^{12}$C, ^{14}N$(p,\gamma)^{15}$O, and ^{18}O$(p,\gamma)^{19}$F reactions with the Q values of 15.96, 7.30, and 7.99 MeV, respectively. The contribution of these reactions to the sum peak of the ^{25}Mg$(p,\gamma)^{26}$Al reaction was evaluated by a GEANT4 simulation normalized to the high-energy portion ($E_\gamma > 7$ MeV), which is less than 6%.

The strength of the 189-keV resonance is determined to be $\omega\gamma_{189} = (9.3 \pm 0.7)\times 10^{-7}$ eV, with a sum peak efficiency of 25%. The quoted uncertainty includes the sum peak statistical uncertainty (3%, including the deduction of background), the GEANT4 simulation (3%), the choice of fitting range (1%), the relative stopping power (1.5%), the normalization to $\omega\gamma_{304}$ (3.2%), as well as the stoichiometry change of ^{25}Mg target (5%). Our strength value for this resonance agrees well with that of $(9.0 \pm 0.8)\times 10^{-7}$ eV determined in the previous underground work [28], while it is 26% higher than the value $(7.4 \pm 1.2)\times 10^{-7}$ eV of Ref. [23], although consistent within the uncertainty.

By using the fitting procedure described in Sec. III A, the primary γ-ray branching ratios of the 189-keV resonance were obtained and are compared to the previous values in Table II. The present ratios are generally consistent with the previous ones. Furthermore, a complete decay scheme is constructed with known branching ratios of secondary transitions taken from [49], which leads to the ground-state feeding factors of $f_0^{189} = (76 \pm 4)\%$. The uncertainty consists of the statistical uncertainty (1%) and the range choice of the gate (5%). Our ground-state feeding factor for this resonance is in good agreement with the LUNA value of $75 \pm 2\%$ [28], but different to the 66% reported in Refs. [24,50].

C. The 130-keV resonance

The 130-keV resonance measurement was performed by bombarding the ^{25}Mg isotope targets with a proton energy of $E_p = 148.3$ keV and considering the 12 keV energy loss in the Cr layer. The background was obtained by using the natural magnesium target under the same beam conditions. Figure 5 shows the summing γ-ray spectrum obtained with an accumulated proton exposure of 110 C, in which the brown shaded area represents the charge-normalized background. The major background was found to be the ^{18}O$(p,\gamma)^{19}$F reaction.

Within the sum peak of the 130-keV resonance, the significant background from the 151-keV resonance in the ^{18}O$(p,\gamma)^{19}$F reaction prevented us from obtaining an effective single spectrum. Consequently, the primary γ-ray branching ratios of the 130-keV resonance obtained in Ref. [20] were adopted to reconstruct the sum spectrum with 40% efficiency in a large region of interest range from 5 to 7 MeV. The sum spectrum, together with the beam-induced background, is then set as the prior probability in Bayesian analysis to calculate the posterior distribution, i.e., the strength of the 130-keV resonance. The best-fitted contribution of the 130-keV resonance based on the total and background spectra are shown in Fig. 5, and the posterior distribution of $\omega\gamma_{130}$ is shown in Fig. 6.

Using the global mode result of the Bayesian posterior distribution, and considering the presence of 10% ^{25}Mg isotope in the natural Mg target, the strength of the 130-keV resonance was determined to be $\omega\gamma_{130} = (1.8 \pm 1.3)\times 10^{-10}$ eV for the first time. Our result agrees with the previous LUNA upper limit of $\omega\gamma_{130} < 2.5\times 10^{-10}$ eV [28], and $\omega\gamma_{130} <$

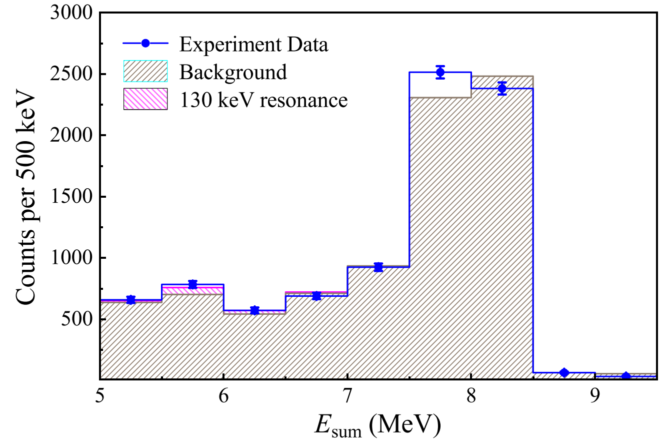

FIG. 5. The blue filled circles show the summing γ-ray spectrum of the 130-keV resonance. The brown shaded area represents the background measured with natural Mg targets, and the pink shaded area shows the Bayesian fitted contribution of the 130-keV resonance.

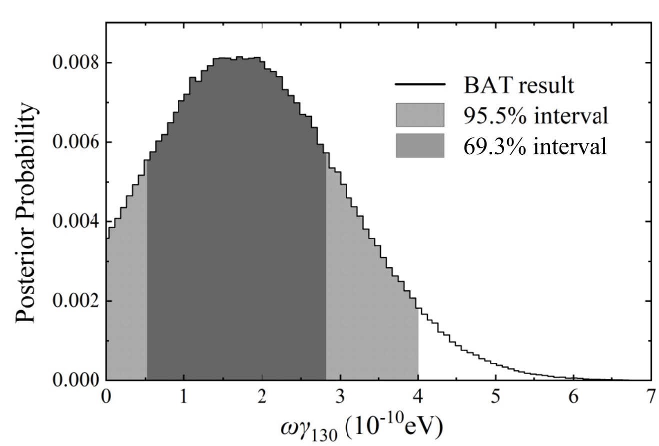

FIG. 6. Posterior probability density function for the 130-keV resonance strength.

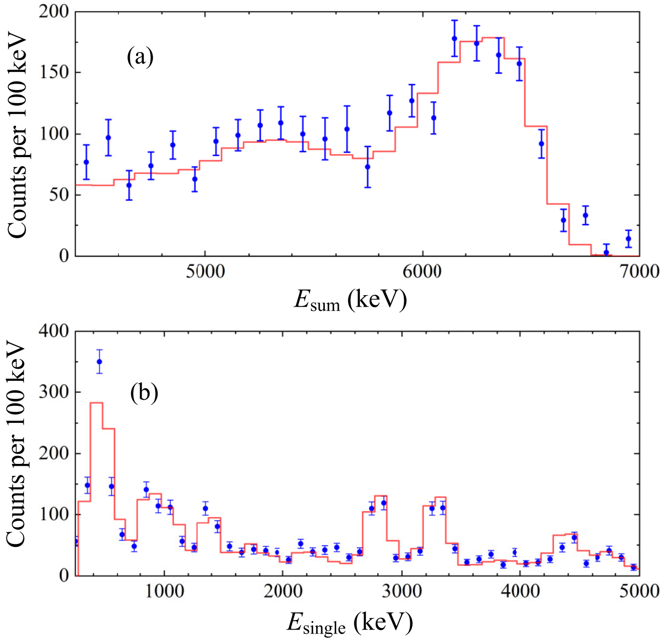

FIG. 7. γ-ray spectra of the 92-keV resonance (in blue circles). (a) Sum spectrum after background subtraction; (b) single spectrum. The line represents the GEANT4 simulation using the primary γ-ray branching ratios extracted from the single spectrum with the Bayesian method.

1.4×10^{-10} eV from the NACRE compilation [29], within the uncertainty. The present result constrains the reaction rate based on more solid experimental ground.

D. The 92-keV resonance

For the 92-keV resonance, the measurement took about six days in an accumulated charge of 1040 C. The proton beam energy was selected as 117.3 keV by considering the 13 keV energy loss in the Cr layer. Figure 7 shows the γ-ray spectra of the 92-keV resonance after background subtraction [36]. We reanalyzed the experimental data using the Bayesian method and compared the obtained primary γ-ray branching ratios to our previous result [36] in Table III. It can be seen that the two results are in good agreement except for the small difference in the transition to the ground state. Based on the present result, the ground-state feeding factor f_0^{92} is determined to be 0.64 ± 0.04, agreeing well with our previous value of 0.66 ± 0.04 [36]. The sources of uncertainty are listed as follows: (1) statistical error (3%), (2) the region choice of gate window (3%), (3) the transitions to other states in ^{26}Al which are not involved in the present primary γ-ray branching ratios (4%). The present f_0^{92} is consistent with the reported values of 0.76 ± 0.10 [31], $0.6^{-0.1}_{+0.2}$ [28], and 0.80 ± 0.15 [17] within the uncertainties, and roughly agrees with the value of 0.52 ± 0.06 [51] within 2σ uncertainty. However, our result has an improved precision by factors of 1.5–4.0.

TABLE III. Primary γ-ray branching ratios for the 92-keV resonance of the ^{25}Mg$(p,\gamma)^{26}$Al reaction.

E_x	Present	Previous [36]	Ref. [31]	Ref. [30]	Ref. [17]
5142	7 ± 2	7 ± 2	1.12 ± 0.39	0.69 ± 0.12	9 ± 3
3403		<1			4 ± 2
3160	53 ± 2	55 ± 2	54.3 ± 1.1	35.5 ± 1.7	76 ± 8
2069	31 ± 2	28 ± 2	15.4 ± 0.4	51.2 ± 2.3	<2
1851					5 ± 2
1759	7 ± 2	8 ± 3	29.1 ± 1.2	12.7 ± 0.7	
0	2 ± 1	<1			4 ± 2

TABLE IV. Parameters used in the present ^{25}Mg$(p,\gamma)^{26}$Al reaction rate calculations.

E_R (keV)[a]	$\omega\gamma$ (eV)	f_0	f_{es}
37.2 ± 0.1	$(4.5 \pm 1.8)\times10^{-22}$[b]	0.79 ± 0.05[b]	
57.7 ± 0.1	$(2.9 \pm 0.5)\times10^{-13}$[c]	0.81 ± 0.05[b]	
92.3 ± 0.2	$(3.7 \pm 0.3)\times10^{-10}$[d]	0.64 ± 0.04[d]	1.25 ± 0.08
130.1 ± 0.1	$(1.8 \pm 1.3)\times10^{-10}$[d]	0.73 ± 0.01[e]	1.14 ± 0.04
189.6 ± 0.1	$(9.3 \pm 0.7)\times10^{-7}$[d]	0.76 ± 0.02[d]	1.08 ± 0.02
304.1 ± 0.1	$(3.1 \pm 0.1)\times10^{-2}$[f]	0.86 ± 0.01[f]	1.04 ± 0.01
374.1 ± 0.1	$(6.6 \pm 0.6)\times10^{-2}$[g]	0.67 ± 0.01[g]	1.03 ± 0.01

[a]Calculated with the level energies and S_p value taken from Ref. [49].
[b]From Ref. [53].
[c]From Ref. [54].
[d]From the present work.
[e]From Ref. [20].
[f]From Ref. [27].
[g]From Ref. [55].

The strength of the 92-keV resonance was derived to be $\omega\gamma_{92} = (3.7 \pm 0.3)\times10^{-10}$ eV. This result is slightly higher than our previous value $(3.6 \pm 0.3)\times10^{-10}$ eV [36] due to a lower sum peak efficiency of 25%. The uncertainty comes from: (1) statistical error including the subtraction of beam-induced background (4%), (2) the region choice of sum peak (3%), (3) the sum peak efficiencies η_{304}/η_{92} (3%), (4) the ratio of effective stopping power $\varepsilon_{eff}(92)/\varepsilon_{eff}(304)$ (0.7%), (5) the uncertainty of the 304-keV resonance strength (3%), (6) the stoichiometry change of the targets (5%). Our strength value for this resonance is consistent with the previous LUNA direct measurement value of $(2.9 \pm 0.6)\times10^{-10}$ eV [28], but with a factor of 2 improved precision. It is 2.2 times greater than the value of 1.16×10^{-10} eV derived from the transfer-reaction experiment [24].

E. Reaction rate

For the narrow and isolated resonances, the reaction cross section can be expressed by the Breit-Wigner approximation, accordingly, the astrophysical reaction rates can be calculated by [48]

$$N_A\langle\sigma v\rangle = \sum_i N_A \left(\frac{2\pi}{\mu kT}\right)^{3/2} \hbar^2 e^{-E_R^i/kT} f_0^i \omega\gamma_i f_{es}, \quad (5)$$

where N_A and k represent the Avogadro's and Boltzmann's constants, μ is the reduced mass, T is the stellar temperature, E_R^i is the resonant energy of the ith resonance in center-of-mass system, and f_0^i is the ground-state feeding

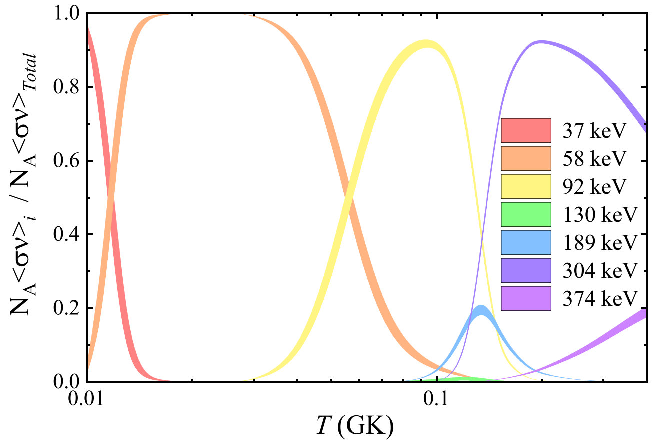

FIG. 8. The proportion of each major resonance in the total $^{25}Mg(p,\gamma)^{26}Al$ rate. The corresponding ±1 σ error bands are shown.

factor. Furthermore, the electron screening effect enhancement factors f_{es} are calculated as $\exp(\pi\eta U_e/E_R^i)$, where η and U_e are the Sommerfeld parameter and the screening potential with a value of 1.14 keV [52], respectively. To calculate the $^{25}Mg(p,\gamma)^{26}Al$ reaction rates, we used our updated $\omega\gamma$ and f_0 values for the 92, 130, and 189 keV resonances, together with the parameters from the previous work listed in Table IV. The resonance parameters not mentioned in the table are taken from Ref. [50].

Our total reaction rate and those for the ground state and the isomeric state, calculated via the Monte Carlo method are listed in Table V, while the contributions of individual resonances are shown in Fig. 8. For the temperature range $0.05 \leqslant T_9 \leqslant 0.3$, the reaction rate is dominated by the 92, 189, and 304 keV resonances whose strengths are precisely determined in the present and our previous work [27]. Here, we confirm that the contribution of the 130-keV resonance is indeed negligible.

Figure 9 shows the present JUNA total reaction rate compared with the results of LUNA [53], Iliadis *et al.* [50], and NACRE [29]. The JUNA reaction rate is 39%, 92%, and 93% higher than those reported by LUNA [53], Iliadis *et al.* [50], and NACRE [29] at 0.09 GK, respectively. The difference of JUNA and LUNA is mainly due to the 32% enhancement of the 92-keV resonance strength. Since the present strength values for the dominant 92, 189, and 304 keV resonances are quite similar to our previous report [36], the present rates and the associated uncertainties are almost identical to the previous ones (please see Ref. [36] for more discussions).

TABLE V. Present reaction rates of $^{25}Mg(p,\gamma)^{26}Al$ expressed in the 10^n scale (in units of $cm^3\ mol^{-1}\ s^{-1}$). The ground-state contribution is calculated by Eq. (5), while the isomeric-state contribution is also calculated by Eq. (5) but replacing f_0 with $(1 - f_0)$.

T_9	Total	Ground state	Isomeric state	n
0.010	1.34 ± 0.52	1.06 ± 0.42	0.28 ± 0.13	−32
0.011	7.19 ± 2.30	5.71 ± 1.84	1.48 ± 0.57	−31
0.012	3.40 ± 0.64	2.73 ± 0.52	0.67 ± 0.18	−29
0.013	1.53 ± 0.24	1.24 ± 0.21	0.29 ± 0.08	−27
0.014	4.96 ± 0.83	4.01 ± 0.71	0.94 ± 0.29	−26
0.015	1.06 ± 0.18	0.86 ± 0.16	0.20 ± 0.06	−24
0.016	1.55 ± 0.27	1.26 ± 0.23	0.29 ± 0.09	−23
0.018	1.36 ± 0.23	1.10 ± 0.20	0.26 ± 0.08	−21
0.020	4.77 ± 0.82	3.87 ± 0.71	0.91 ± 0.29	−20
0.025	2.76 ± 0.48	2.24 ± 0.41	0.52 ± 0.17	−17
0.03	1.83 ± 0.31	1.48 ± 0.27	0.35 ± 0.11	−15
0.04	3.29 ± 0.54	2.64 ± 0.47	0.65 ± 0.19	−13
0.05	8.64 ± 1.13	6.67 ± 0.97	1.98 ± 0.40	−12
0.06	1.06 ± 0.10	0.77 ± 0.08	0.29 ± 0.04	−10
0.07	7.92 ± 0.70	5.49 ± 0.55	2.43 ± 0.34	−10
0.08	3.89 ± 0.36	2.64 ± 0.28	1.25 ± 0.18	−9
0.09	1.38 ± 0.13	0.93 ± 0.10	0.45 ± 0.07	−8
0.10	3.85 ± 0.36	2.58 ± 0.28	1.27 ± 0.19	−8
0.11	9.32 ± 0.83	6.30 ± 0.64	3.02 ± 0.43	−8
0.12	2.19 ± 0.17	1.52 ± 0.13	0.66 ± 0.09	−7
0.13	5.81 ± 0.31	4.32 ± 0.24	1.49 ± 0.15	−7
0.14	1.88 ± 0.07	1.50 ± 0.06	0.38 ± 0.03	−6
0.15	6.72 ± 0.24	5.62 ± 0.21	1.10 ± 0.07	−6
0.16	2.33 ± 0.09	1.99 ± 0.08	0.34 ± 0.02	−5
0.18	2.08 ± 0.08	1.80 ± 0.08	0.28 ± 0.02	−4
0.20	1.24 ± 0.05	1.08 ± 0.05	0.16 ± 0.01	−3
0.25	3.16 ± 0.13	2.73 ± 0.11	0.43 ± 0.03	−2
0.30	2.72 ± 0.10	2.34 ± 0.09	0.39 ± 0.03	−1
0.35	1.28 ± 0.05	1.09 ± 0.04	0.19 ± 0.01	0
0.40	4.10 ± 0.15	3.45 ± 0.13	0.64 ± 0.04	0
0.45	1.03 ± 0.04	0.86 ± 0.03	0.17 ± 0.01	1
0.50	2.15 ± 0.08	1.78 ± 0.07	0.37 ± 0.02	1
0.60	6.72 ± 0.25	5.45 ± 0.21	1.26 ± 0.07	1
0.70	1.55 ± 0.06	1.23 ± 0.05	0.32 ± 0.02	2
0.80	2.94 ± 0.12	2.30 ± 0.09	0.64 ± 0.04	2
0.90	4.89 ± 0.21	3.76 ± 0.16	1.13 ± 0.07	2
1.00	7.41 ± 0.33	5.61 ± 0.24	1.80 ± 0.11	2
1.25	1.60 ± 0.08	1.17 ± 0.05	0.43 ± 0.03	3
1.50	2.73 ± 0.13	1.96 ± 0.09	0.77 ± 0.05	3
1.75	4.07 ± 0.19	2.87 ± 0.13	1.20 ± 0.07	3
2.00	5.57 ± 0.25	3.87 ± 0.17	1.69 ± 0.09	3

IV. ASTROPHYSICAL IMPLICATION

Our updated $^{25}Mg(p,\gamma)^{26}Al$ reaction rate is maximally enhanced at around 0.09 GK, which can be reached at the base of the convective envelope for low-metallicity massive AGB star. To assess the impact of the present new reaction rate on the ^{26}Al yield, a one-dimensional open-source stellar evolution code MESA (Modules for Experiments in Stellar Astrophysics [56–60], version r15140) is used to evolve a $5\ M_\odot$ star with low metallicity of $Z = 0.001$ from the zero-age main sequence to the end of the AGB phase, defined as the time when the mass of the convective envelope has decreased to $0.01\ M_\odot$. The mass loss by winds on the RGB is modeled by using the Reimers approximation [61], and the Blöcker law [62] is used on the AGB.

While AGB stars of high mass and low metallicity are not a potential significant source of the currently observed ^{26}Al in the galaxy (in fact, the typical current metallicity range in the galaxy is about twice higher and lower than solar), we have chosen a $M = 5\,M_\odot$, $Z = 0.001$ star as an example here to

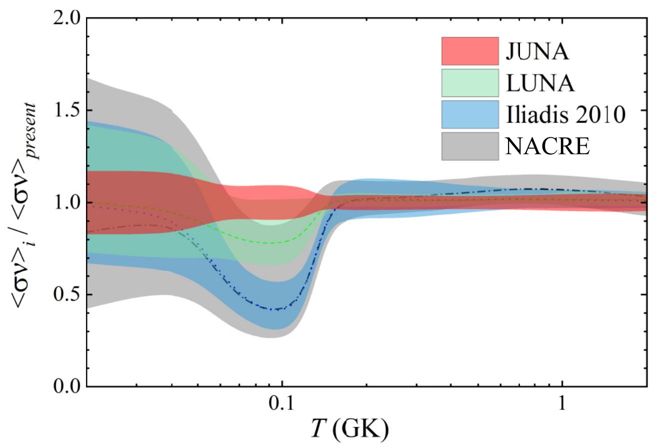

FIG. 9. Comparison between the present total $^{25}Mg(p,\gamma)^{26}Al$ reaction rate and those of LUNA [53] (green line), Iliadis *et al.* [50] (blue line), and NACRE [29] (grey line). The shaded bands represent the corresponding 1σ uncertainties.

show the effect of our new rate because such a star is hotter than its counterpart at solar metallicity therefore this effect can be shown more clearly. Nevertheless, such stars are interesting because they are possible polluters of globular clusters [8] and they may have produced stardust grains that are found in meteorites [7].

The network contains neutron and the following 42 isotopes: ^{1-2}H, ^{3-4}He, ^{6-7}Li, ^{7-8}Be, ^{8}B, $^{12-13}C$, $^{13-15}N$, $^{15-18}O$, $^{17-19}F$, $^{20-22}Ne$, $^{21-23}Na$, $^{24-26}Mg$, $^{25,27}Al$, $^{27-30}Si$, ^{31}P, ^{32}S, ^{36}Ar, ^{40}Ca, together with the ground and isomeric states of ^{26}Al. The communications between the ground and isomeric states of ^{26}Al are taken into account, but the calculations show that it does not influence the evolution of ^{26}Al due to the low temperature concerned in the present model. Other isotopes and reactions, which are not included in the calculation, only produce negligible energy and do not affect the stellar structure [63]. Nuclear reaction rates are from NACRE [29], except for the $^{14}N(p,\gamma)^{15}O$ reaction rate, we have updated to the most recent Frentz *et al.* [64] rate.

Figure 10 shows the evolution of the convective regions for the 5 $M_\odot$ AGB star model calculation, focusing on the bottom of the convective envelope. Helium(He)-intershell is located between the yellow solid line and red dotted line, which is surrounded by a large hydrogen rich convective envelope. The teardrop-shaped pockets are periodic thermal pulses caused by instabilities in the thin He-burning shell, drive pulse convective zones, which mix ashes from the He-burning shell into the He-intershell. The convective envelope later goes inward and carries He-burning shell material to the surface of the star, which is called the third dredge-up (TDU) [65].

Figure 11 shows the temperature at the base of the convective envelope (T_{BCE}) and the effective temperature on the stellar surface (T_{eff}) during the AGB phase. The temperature at the base of the convective envelope can reach as high as 0.09 GK, which is high enough to activate the CNO cycle, and even the NeNa and MgAl cycles, known as the hot bottom burning (HBB) mechanism [66]. The expansion of the stellar layers above the carbon core lowers T_{BCE} and extinguishes the HBB process when T_{BCE} reduces to the minimum requirement of 0.04 GK [67]. The HBB and TDU processes occur separately in time from each other.

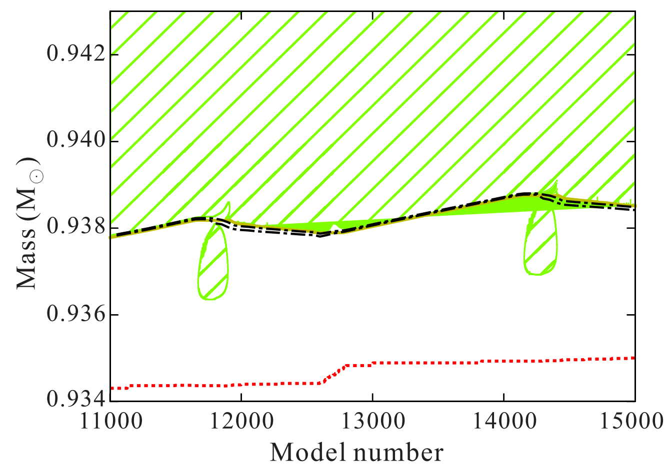

FIG. 10. Evolution of the convective regions on the bottom of the convective envelope for the 5 $M_\odot$ star of metallicity $Z = 0.001$. The x axis is evolution model number, which is a proxy for time. The green dashed areas correspond to convection. The yellow solid line indicates the hydrogen-depleted core, or helium core, where the hydrogen mass fraction is below 0.01 and the ^4He mass fraction is above 0.1. The red dotted line indicates the same as the yellow solid line but with helium and carbon. The black dash dotted lines are the borders of the region where the temperature is between 0.07 GK and 0.09 GK. The teardrop-shaped pockets correspond to the flash-driven convective region.

By the HBB and TDU processes, the AGB star carries the products of internal H-burning materials and He-burning shell materials to the surface of stars. These materials are ejected by the strong wind and enrich the interstellar medium from which the next generation of stars are formed, and contribute to the chemical evolution of galaxies [68]. Variation in elemental abundance depends especially on mixing, as well as

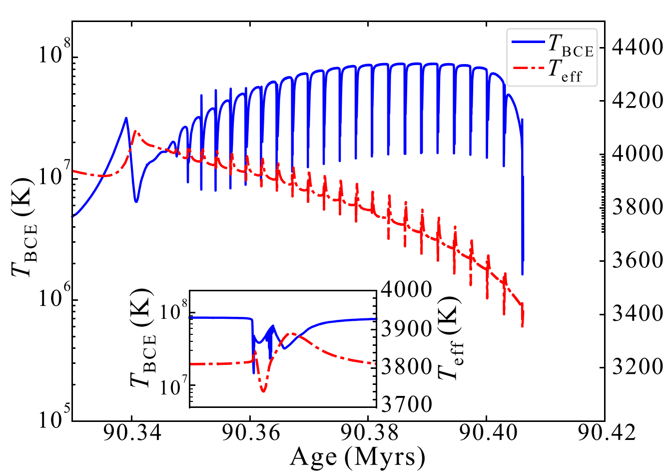

FIG. 11. The temperatures at the base of the convective envelope T_{BCE} (in blue line) and on the stellar surface T_{eff} (in red line) during the AGB phase. The 14th TP is zoomed in the inset.

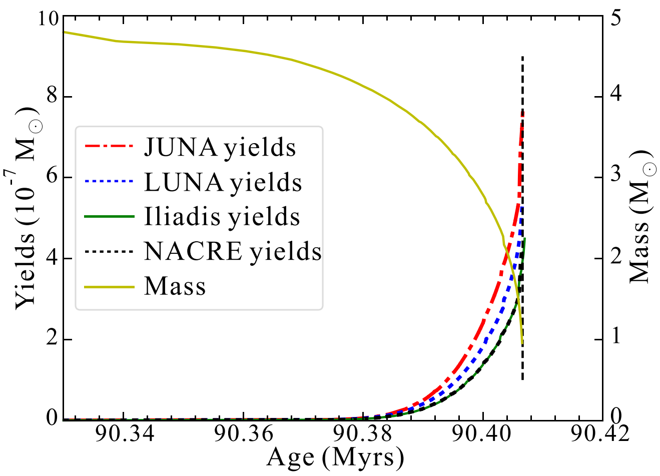

FIG. 12. The $^{26}Al^g$ yields (on the left y axis) and the stellar mass (on the right y axis) as a function of the star age on its AGB phase. The red dash-dotted line, blue dotted line, green solid line, and black dotted line represent the $^{26}Al^g$ yields obtained by using the present, LUNA [53], Iliadis *et al.* [50], and NACRE [29] rates for the $^{25}Mg(p,\gamma)^{26}Al$ reaction, respectively. The orange solid line represents the evolution of the star mass. The vertical dashed line indicates the end of the evolution where the mass of the convective envelope is less than 0.01 M$_\odot$.

the adopted mass-loss rates and reaction rates. In the present calculations, only the reaction rates of $^{25}Mg(p,\gamma)^{26}Al$ are changed. Therefore, variations of the surface abundances in our models are caused only by the difference in the $^{25}Mg(p,\gamma)^{26}Al$ reaction rates.

Neutrons provided by the $^{22}Ne(\alpha,n)^{25}Mg$ reaction in the thermal pulses trigger the $^{26}Al^g$ destruction via the $^{26}Al(n,p)^{26}Mg$ and $^{26}Al(n,\alpha)^{22}Ne$ reactions [69], and hence $^{26}Al^g$ is mainly produced at the base of the convective envelope by HBB process. The consumed ^{25}Mg is replenished by the fresh ^{25}Mg from the large H-shell convective envelope, and hence the $^{25}Mg(p,\gamma)^{26}Al$ reaction does not significantly affect the ^{25}Mg abundance. Therefore, the $^{26}Al^g$ yields should be proportional to the $^{25}Mg(p,\gamma)^{26}Al$ reaction rates, as found by Izzard *et al.* [11] in AGB stars with mass between 4 M$_\odot$ and 6 M$_\odot$ and with metallicities between $Z = 0.0001$ and 0.02.

Figure 12 shows the predicted yields of $^{26}Al^g$ by using four different $^{25}Mg(p,\gamma)^{26}Al$ reaction rates. The yields of $^{26}Al^g$ increase with the evolution of the star, its radioactive decay can be ignored within such a short time scale. The results indicate that the present $^{25}Mg(p,\gamma)^{26}Al$ rate increases the $^{26}Al^g$ yields at the end of the evolution by about 45%, 71%, 79% compared to those using the LUNA, Iliadis *et al.* [50] and NACRE rates, respectively. It can be seen from Fig. 11 that the star spends most of the time at T_{BCE} between 0.07–0.09 GK during the AGB phase. The present $^{25}Mg(p,\gamma)^{26}Al$ reaction rate is enhanced about 32%, 65%, and 70% at 0.07 GK, 39%, 92%, and 93% at 0.09 GK compared to LUNA, Iliadis *et al.* [50], and NACRE rates, respectively. Therefore, the enhancement of the present $^{26}Al^g$ yields is roughly proportional to the $^{25}Mg(p,\gamma)^{26}Al$ reaction rates in the temperature region of 0.07–0.09 GK as predicted before [11]. Nuclear reaction rates are from NACRE [29], except for the $^{14}N(p,\gamma)^{15}O$ reaction rate, we have updated to the most recent Frentz *et al.* [64] rate. Changing all the other reactions rates from NACRE to the JINA [70] did not have any significant impact on our results.

In addition, our calculations show that the 5 M$_\odot$ star of metallicity $Z = 0.001$ has O-rich surface (O > C), the condition for formation of the oxide and silicate grains. Compared to the LUNA rate, our updated rate shows almost no change for ^{24}Mg, ^{26}Mg, and ^{27}Al yields, hence the change of $^{26}Al/^{27}Al$ ratio equals to the change of ^{26}Al which increases about 45%. This may help to explain the high $^{26}Al/^{27}Al$ ratios of stardust grains [7]. As for the Al/Mg ratio, which is the observable in globular clusters [8], its changes are negligible in our model calculations.

V. SUMMARY

We have measured the $E_{c.m.} = 92$, 130, and 189 keV resonances in the $^{25}Mg(p,\gamma)^{26}Al$ reaction at CJPL. Their resonance strengths were determined relative to that of the well-known 304-keV resonance by a thick-target method. The primary γ-ray branching ratios of the 92, 189, and 304 keV resonances were extracted from the single spectrum. These ratios agree with the previous results. In addition, the ground-state feeding factors for the 92 and 189 keV resonances have been deduced, also consistent with the previous ones. Based on the JUNA data, a most precise $^{25}Mg(p,\gamma)^{26}Al$ rate has been determined so far. The present rate is enhanced by 32% to 93% in the temperature region of 0.07–0.09 GK compared with the previous works.

The astrophysical impact of the new rates on the ^{26}Al yield has been investigated with the MESA code. The calculation focus on a 5 M$_\odot$ AGB star with a low metallicity $Z = 0.001$, which experiences a HBB process at the base of the convective envelope to activate the MgAl cycle. It shows that the present $^{25}Mg(p,\gamma)^{26}Al$ rates increase about (45–79)% of ^{26}Al yield compared to the previous rates, and the variation in the $^{26}Al^g$ yield is roughly proportional to the $^{25}Mg(p,\gamma)^{26}Al$ reaction rate. A reduced effect of the rate on the yield of $^{26}Al^g$ is expected for the lower mass and higher metallicity AGB stars, which have relatively lower T_{BCE} than the model considered here. More comprehensive studies are needed to fully evaluate the impact of this $^{25}Mg(p,\gamma)^{26}Al$ new rate in AGB stars, and in the stardust grains that are found in meteorites. Furthermore, the uncertainty of one of the main destruction channels of $^{26}Al^g$, the $^{26}Al(p,\gamma)^{27}Si$ reaction at temperatures around 0.06–0.1 GK [15] is still rather large. Direct measurements of this destruction reaction are strongly desired in both above-ground and underground laboratories.

ACKNOWLEDGMENTS

The authors are very grateful to the anonymous referee who provided valuable comments and suggestions. We also thank the staff of the CJPL and Yalong River Hydropower Development Company and Tsinghua University for laboratory support. The present work is supported by the National Natural Science Foundation of China (Grants No. 12175152, No. 12275026, No. 11775133, No. 11490563, No. U1867211, No. 11961141003, No. 11905136, and No. 11405096), the Continuous Basic Scientific Research Projects No. WDJC-2019-13 and No. BJ20002501, the equipment research and development project of Chinese Academy of Sciences (Grant No. 28Y531040), and research fund of CNNC.

[1] W. A. Mahoney, J. C. Ling, A. S. Jacobson, and R. E. Lingenfelter, Diffuse galactic gamma-ray line emission from nucleosynthetic ^{60}Fe, ^{26}Al, and ^{22}Na: Preliminary limits from HEAO 3, Astrophys. J. **262**, 742 (1982).

[2] R. Diehl, C. Dupraz, K. Bennett, H. Bloemen, W. Hermsen, J. Knöedlseder, G. Lichti, D. Morris, J. Ryan, V. Schöenfelder *et al.*, COMPTEL observations of galactic ^{26}Al emission, Astron. Astrophys. **298**, 445 (1995).

[3] R. Diehl, H. Halloin, K. Kretschmer, G. G. Lichti, V. Schönfelder, A. W. Strong, A. von Kienlin, W. Wang, P. Jean, J. Knödlseder *et al.*, Radioactive ^{26}Al from massive stars in the Galaxy, Nature (London) **439**, 45 (2006).

[4] T. Lee, D. A. Papanastassiou, and G. J. Wasserburg, Aluminum-26 in the early solar system: Fossil or fuel? Astrophys. J. Lett. **211**, L107 (1977).

[5] E. Groopman, E. Zinner, S. Amari, F. Gyngard, P. Hoppe, M. Jadhav, Y. Lin, Y. Xu, K. Marhas, and L. R. Nittler, Inferred initial ^{26}Al/^{27}Al ratios in presolar stardust grains from supernovae are higher than previously estimated, Astrophys. J. **809**, 31 (2015).

[6] M. Lugaro, U. Ott, and Á. Kereszturi, Radioactive nuclei from cosmochronology to habitability, Prog. Part. Nucl. Phys. **102**, 1 (2018).

[7] M. Lugaro, A. I. Karakas, C. G. Bruno, M. Aliotta, L. R. Nittler, D. Bemmerer, A. Best, A. Boeltzig, C. Broggini, A. Caciolli *et al.*, Origin of meteoritic stardust unveiled by a revised proton-capture rate of ^{17}O, Nat. Astron. **1**, 0027 (2017).

[8] S. Mészáros, D. A. García-Hernández, S. Cassisi, M. Monelli, L. Szigeti, F. Dell'Agli, A. Derekas, T. Masseron, M. Shetrone, P. Stetson *et al.*, A photometric study of globular clusters observed by the APOGEE survey, Mon. Not. R. Astron. Soc. **475**, 1633 (2018).

[9] A. Palacios, G. Meynet, C. Vuissoz, J. Knödlseder, D. Schaerer, M. Cerviño, and N. Mowlavi, New estimates of the contribution of Wolf-Rayet stellar winds to the galactic Al, Astron. Astrophys. **429**, 613 (2005).

[10] H. Norgaard, ^{26}Al from red giants, Astrophys. J. **236**, 895 (1980).

[11] R. G. Izzard, M. Lugaro, A. I. Karakas, C. Iliadis, and M. van Raai, Reaction rate uncertainties and the operation of the NeNa and MgAl chains during HBB in intermediate-mass AGB stars, Astron. Astrophys. **466**, 641 (2007).

[12] M. Limongi and A. Chieffi, The nucleosynthesis of ^{26}Al and ^{60}Fe in solar metallicity stars extending in mass from 11 to 120 $M_\odot$: The hydrostatic and explosive contributions, Astrophys. J. **647**, 483 (2006).

[13] H. E. Brinkman, C. L. Doherty, O. R. Pols, E. T. Li, B. Côté, and M. Lugaro, Aluminium-26 from massive binary stars. I. Nonrotating models, Astrophys. J. **884**, 38 (2019).

[14] H. E. Brinkman, J. W. den Hartogh, C. L. Doherty, M. Pignatari, and M. Lugaro, ^{26}Aluminum from massive binary stars. II. Rotating single stars up to core collapse and their impact on the early solar system, Astrophys. J. **923**, 47 (2021).

[15] A. M. Laird, M. Lugaro, A. Kankainen, P. Adsley, D. Bardayan, H. Brinkman, B. Côté, C. Deibel, R. Diehl, F. Hammache *et al.*, Progress on nuclear reaction rates affecting the stellar production of ^{26}Al, J. Phys. G: Nucl. Part. Phys. **50**, 033002 (2023).

[16] R. Betts, H. Fortune, and D. Pullen, A study of ^{26}Al by the ^{25}Mg(^{3}He, d) reaction, Nucl. Phys. A **299**, 412 (1978).

[17] A. Champagne, A. Howard, and P. Parker, Threshold states in ^{26}Al: (I). Experimental investigations, Nucl. Phys. A **402**, 159 (1983).

[18] P. Endt, P. De Wit, and C. Alderliesten, The ^{25}Mg$(p,\gamma)^{26}$Al and the ^{25}Mg(p,p') resonances for $E_p = 0.31$–1.84 MeV, Nucl. Phys. A **459**, 61 (1986).

[19] A. Champagne, A. McDonald, T. Wang, A. Howard, P. Magnus, and P. Parker, Threshold states in ^{26}Al revisited, Nucl. Phys. A **451**, 498 (1986).

[20] P. Endt, P. De Wit, and C. Alderliesten, The ^{25}Mg$(p,\gamma)^{26}$Al reaction; branchings, energies and lifetimes, Nucl. Phys. A **476**, 333 (1988).

[21] A. Champagne, A. Howard, M. Smith, P. Magnus, and P. Parker, The effect of weak resonances on the ^{25}Mg$(p,\gamma)^{26}$Al reaction rate, Nucl. Phys. A **505**, 384 (1989).

[22] A. Rollefson, V. Wijekumar, C. Browne, M. Wiescher, H. Hausman, W. Kim, and P. Schmalbrock, Spectroscopic factors for proton unbound levels in ^{26}Al and their influence on stellar reaction rates, Nucl. Phys. A **507**, 413 (1990).

[23] C. Iliadis, T. Schange, C. Rolfs, U. Schröder, E. Somorjai, H. P. Trautvetter, K. Wolke, P. M. Endt, S. W. Kikstra, A. E. Champagne *et al.*, Low-energy resonances in ^{25}Mg$(p,\gamma)^{26}$Al, ^{26}Mg$(p,\gamma)^{27}$Al and ^{27}Al$(p,\gamma)^{28}$Si, Nucl. Phys. A **512**, 509 (1990).

[24] C. Iliadis, L. Buchmann, P. M. Endt, H. Herndl, and M. Wiescher, New stellar reaction rates for ^{25}Mg$(p,\gamma)^{26}$Al and ^{25}Al(p, γ)^{26}Si, Phys. Rev. C **53**, 475 (1996).

[25] D. Powell, C. Iliadis, A. Champagne, S. Hale, V. Hansper, R. Surman, and K. Veal, Low-energy resonance strengths for proton capture on Mg and Al nuclei, Nucl. Phys. A **644**, 263 (1998).

[26] B. Limata, F. Strieder, A. Formicola, G. Imbriani, M. Junker, H. W. Becker, D. Bemmerer, A. Best, R. Bonetti, C. Broggini *et al.* (LUNA Collaboration), New experimental study of low-energy (p,γ) resonances in magnesium isotopes, Phys. Rev. C **82**, 015801 (2010).

[27] H. Zhang, Z. H. Li, J. Su, Y. J. Li, C. Chen, L. Zhang, F. Q. Cao, Y. P. Shen, W. Nan, W. K. Nan *et al.*, Direct measurement of the resonance strengths and branching ratios for the low-energy (p,γ) reactions on Mg isotopes, Chin. Phys. C **45**, 084108 (2021).

[28] F. Strieder, B. Limata, A. Formicola, G. Imbriani, M. Junker, D. Bemmerer, A. Best, C. Broggini, A. Caciolli, P. Corvisiero *et al.*, The ^{25}Mg$(p,\gamma)^{26}$Al reaction at low astrophysical energies, Phys. Lett. B **707**, 60 (2012).

[29] C. Angulo, M. Arnould, M. Rayet, P. Descouvemont, D. Baye, C. Leclercq-Willain, A. Coc, S. Barhoumi, P. Aguer, C. Rolfs *et al.*, A compilation of charged-particle induced thermonuclear reaction rates, Nucl. Phys. A **656**, 3 (1999).

[30] A. Kankainen, P. J. Woods, D. T. Doherty, H. M. Albers, M. Albers, A. D. Ayangeakaa, M. P. Carpenter, C. J. Chiara, J. L.

Harker, R. V. F. Janssens *et al.*, Decay of the key 92-keV resonance in the ^{25}Mg(p, γ) reaction to the ground and isomeric states of the cosmic γ-ray emitter ^{26}Al, Phys. Lett. B **813**, 136033 (2021).

[31] G. Lotay, D. T. Doherty, R. V. F. Janssens, D. Seweryniak, H. M. Albers, S. Almaraz-Calderon, M. P. Carpenter, A. E. Champagne, C. J. Chiara, C. R. Hoffman *et al.*, Revised decay properties of the key 93 keV resonance in the ^{25}Mg(p, γ) reaction and its influence on the MgAl cycle in astrophysical environments, Phys. Rev. C **105**, L042801 (2022).

[32] W. P. Liu, Z. H. Li, J. J. He, X. D. Tang, G. Lian, Z. An, J. J. Chang, H. Chen, Q. H. Chen, X. J. Chen *et al.* (JUNA Collaboration), Progress of Jinping underground laboratory for nuclear astrophysics (JUNA), Sci. China-Phys. Mech. Astron. **59**, 642001 (2016).

[33] J. P. Cheng, K. J. Kang, J. M. Li, J. Li, Y. J. Li, Q. Yue, Z. Zeng, Y. H. Chen, S. Y. Wu, X. D. Ji, and H. T. Wong, The china jinping underground laboratory and its early science, Ann. Rev. Nucl. Part. Sci. **67**, 231 (2017).

[34] J. He, S. Xu, S. Ma, J. Hu, L. Zhang, C. Fu, N. Zhang, G. Lian, J. Su, Y. Li *et al.*, A proposed direct measurement of cross section at Gamow window for key reaction ^{19}F(p, α)^{16}O in asymptotic giant branch stars with a planned accelerator in CJPL, Sci. China: Phys., Mech. Astron. **59**, 652001 (2016).

[35] Y. C. Wu, X. Q. Hao, Q. Yue, Y. J. Li, J. P. Cheng, K. J. Kang, Y. H. Chen, J. Li, J. M. Li, and Y.-L. o. Li, Measurement of cosmic ray flux in the China JinPing underground laboratory, Chin. Phys. C **37**, 086001 (2013).

[36] J. Su, H. Zhang, Z. H. Li, P. Ventura, Y. J. Li, E. T. Li, C. Chen, Y. P. Shen, G. Lian, B. Guo *et al.*, First result from the Jinping underground nuclear astrophysics experiment JUNA: Precise measurement of the 92 keV ^{25}Mg(p, γ)^{26}Al resonance, Sci. Bull. **67**, 125 (2022).

[37] Q. Wu, L. Sun, B. Cui, G. Lian, Y. Yang, H. Ma, X. Tang, X. Zhang, Z. Zhang, and W. Liu, Design of an intense ion source and LEBT for Jinping Underground Nuclear Astrophysics experiments, Nucl. Instrum. Methods Phys. Res. A **830**, 214 (2016).

[38] L. Y. Zhang, J. Su, J. J. He, M. Wiescher, R. J. deBoer, D. Kahl, Y. J. Chen, X. Y. Li, J. G. Wang, L. Zhang *et al.*, Direct Measurement of the Astrophysical ^{19}F($p, \alpha\gamma$)^{16}O Reaction in the Deepest Operational Underground Laboratory, Phys. Rev. Lett. **127**, 152702 (2021).

[39] L. Y. Zhang, J. J. He, R. J. deBoer, M. Wiescher, A. Heger, D. Kahl, J. Su, D. Odell, Y. J. Chen, X. Y. Li *et al.*, Measurement of ^{19}F(p, γ)^{20}Ne reaction suggests CNO breakout in first stars, Nature (London) **610**, 656 (2022).

[40] S. Wang *et al.*, Nucl. Instrum. Methods Phys. Res. A, to be submitted.

[41] C. Chen, Y. J. Li, H. Zhang, and Z. H. Li, Nucl. Sci. Tech. **31**, 91 (2020).

[42] J. F. Ziegler, M. D. Ziegler, and J. P. Biersack, SRIM–the stopping and range of ions in matter (2010), Nucl. Instrum. Methods Phys. Res. B **268**, 1818 (2010).

[43] S. Agostinelli, J. Allison, K. Amako, J. Apostolakis, H. Araujo, P. Arce, M. Asai, D. Axen, S. Banerjee, G. Barrand *et al.*, GEANT4—A simulation toolkit, Nucl. Instrum. Methods Phys. Res. A **506**, 250 (2003).

[44] A. Simon, S. J. Quinn, A. Spyrou, A. Battaglia, I. Beskin, A. Best, B. Bucher, M. Couder, P. A. DeYoung, X. Fang *et al.*, SuN: Summing NaI (Tl) gamma-ray detector for capture reaction measurements, Nucl. Instrum. Methods Phys. Res. A **703**, 16 (2013).

[45] C. S. Reingold, O. Olivas-Gomez, A. Simon, J. Arroyo, M. Chamberlain, J. Wurzer, A. Spyrou, F. Naqvi, A. C. Dombos, A. Palmisano *et al.*, High efficiency total absorption spectrometer hector for capture reaction measurements, Eur. Phys. J. A **55**, 77 (2019).

[46] L. H. Wang, Y. D. Sheng, J. Su, J. J. He, L. Y. Zhang, Z. M. Li, H. Zhang, Y. P. Shen, Z. H. Li, B. Guo *et al.*, γ spectrum analysis for the direct measurement of nuclear astrophysical reaction, J. Beijing Norm. Univ., Nat. Sci. **58**, 748 (2022).

[47] A. Caldwell, D. Kollár, and K. Kröninger, BAT – the Bayesian analysis toolkit, Comput. Phys. Commun. **180**, 2197 (2009).

[48] C. E. Rolfs, W. S. Rodney, and W. S. Rodney, *Cauldrons in the Cosmos: Nuclear Astrophysics* (University of Chicago Press, Chicago, 1988).

[49] M. Basunia and A. Hurst, Nuclear data sheets for A = 26, Nucl. Data Sheets **134**, 1 (2016).

[50] C. Iliadis, R. Longland, A. Champagne, A. Coc, and R. Fitzgerald, Charged-particle thermonuclear reaction rates: II. Tables and graphs of reaction rates and probability density functions, Nucl. Phys. A **841**, 31 (2010).

[51] A. I. Karakas, Updated stellar yields from asymptotic giant branch models, Mon. Not. R. Astron. Soc. **403**, 1413 (2010).

[52] K. N. Huang, M. Aoyagi, M. H. Chen, B. Crasemann, and H. Mark, Neutral-atom electron binding energies from relaxed-orbital relativistic Hartree-Fock-Slater calculations $2 \leqslant Z \leqslant 106$, At. Data Nucl. Data Tables **18**, 243 (1976).

[53] O. Straniero, G. Imbriani, F. Strieder, D. Bemmerer, C. Broggini, A. Caciolli, P. Corvisiero, H. Costantini, S. Cristallo, A. DiLeva *et al.*, Impact of a revised ^{25}Mg(p, γ)^{26}Al reaction rate on the operation of the Mg-Al cycle, Astrophys. J. **763**, 100 (2013).

[54] Y. J. Li, Z. H. Li, E. T. Li, X. Y. Li, T. L. Ma, Y. P. Shen, J. C. Liu, L. Gan, Y. Su, L. H. Qiao *et al.*, Indirect measurement of the 57.7 keV resonance strength for the astrophysical γ-ray source of the ^{25}Mg(p, γ)^{26}Al reaction, Phys. Rev. C **102**, 025804 (2020).

[55] P. Endt, Energy levels of A = 21–44 nuclei (VII), Nucl. Phys. A **521**, 1 (1990).

[56] B. Paxton, L. Bildsten, A. Dotter, F. Herwig, P. Lesaffre, and F. Timmes, Modules for experiments in stellar astrophysics (MESA), Astrophys. J. Supp. Ser. **192**, 3 (2011).

[57] B. Paxton, M. Cantiello, P. Arras, L. Bildsten, E. F. Brown, A. Dotter, C. Mankovich, M. H. Montgomery, D. Stello, F. X. Timmes *et al.*, Modules for experiments in stellar astrophysics (MESA): Planets, oscillations, rotation, and massive stars, Astrophys. J. Supp. Ser. **208**, 4 (2013).

[58] B. Paxton, P. Marchant, J. Schwab, E. B. Bauer, L. Bildsten, M. Cantiello, L. Dessart, R. Farmer, H. Hu, N. Langer *et al.*, Modules for experiments in stellar astrophysics (MESA): Binaries, pulsations, and explosions, Astrophys. J. Supp. Ser. **220**, 15 (2015).

[59] B. Paxton, J. Schwab, E. B. Bauer, L. Bildsten, S. Blinnikov, P. Duffell, R. Farmer, J. A. Goldberg, P. Marchant, E. Sorokina *et al.*, Modules for experiments in stellar astrophysics (MESA): Convective boundaries, element diffusion, and massive star explosions, Astrophys. J. Supp. Ser. **234**, 34 (2018).

[60] B. Paxton, R. Smolec, J. Schwab, A. Gautschy, L. Bildsten, M. Cantiello, A. Dotter, R. Farmer, J. A. Goldberg, A. S. Jermyn *et al.*, Modules for experiments in stellar astrophysics (MESA):

Pulsating variable stars, rotation, convective boundaries, and energy conservation, Astrophys. J. Supp. Ser. **243**, 10 (2019).

[61] B. Baschek, W. H. Kegel, and G. Traving, Problems in Stellar Atmospheres and Envelopes (1975).

[62] T. Blöcker, Stellar evolution of low and intermediate-mass stars. I. Mass loss on the AGB and its consequences for stellar evolution, Astron. Astrophys. **297**, 727 (1995).

[63] C. L. Doherty, P. Gil-Pons, H. H. B. Lau, J. C. Lattanzio, and L. Siess, Super and massive AGB stars – II. Nucleosynthesis and yields – Z = 0.02, 0.008 and 0.004, Mon. Not. R. Astron. Soc. **437**, 195 (2013).

[64] B. Frentz, A. Aprahamian, A. Boeltzig, T. Borgwardt, A. M. Clark, R. J. deBoer, G. Gilardy, J. Görres, M. Hanhardt, S. L. Henderson *et al.*, Investigation of the $^{14}N(p,\gamma)^{15}O$ reaction and its impact on the CNO cycle, Phys. Rev. C **106**, 065803 (2022).

[65] A. I. Karakas and J. C. Lattanzio, The Dawes review 2: Nucleosynthesis and stellar yields of low- and intermediate-mass single stars, Publ. Astron. Soc. Aust. **31**, e030 (2014).

[66] C. K. Fishlock, A. I. Karakas, M. Lugaro, and D. Yong, Evolution and nucleosynthesis of asymptotic giant branch stellar models of low metallicity, Astrophys. J. **797**, 44 (2014).

[67] D. A. García-Hernández, O. Zamora, A. Yagüe, S. Uttenthaler, A. I. Karakas, M. Lugaro, P. Ventura, and D. L. Lambert, Hot bottom burning and *s*-process nucleosynthesis in massive AGB stars at the beginning of the thermally-pulsing phase, Astron. Astrophys. **555**, L3 (2013).

[68] C. Kobayashi, A. I. Karakas, and H. Umeda, The evolution of isotope ratios in the Milky Way Galaxy, Mon. Not. R. Astron. Soc. **414**, 3231 (2011).

[69] U. Battino, C. Lederer-Woods, M. Pignatari, B. Soós, M. Lugaro, D. Vescovi, S. Cristallo, P. J. Woods, and A. Karakas, Impact of newly measured $^{26}Al(n,p)^{26}Mg$ and $^{26}Al(n,\alpha)^{22}Ne$ reaction rates on the nucleosynthesis of ^{26}Al in stars, Mon. Not. R. Astron. Soc. **520**, 2436 (2023).

[70] R. H. Cyburt, A. M. Amthor, R. Ferguson, Z. Meisel, K. Smith, S. Warren, A. Heger, R. D. Hoffman, T. Rauscher, A. Sakharuk *et al.*, The JINA Reaclib database: Its recent updates and impact on type-i x-ray bursts, Astrophys. J. Supp. Ser. **189**, 240 (2010).